Journal of Nuclear Materials 500 (2018) 337–348

Contents lists available at ScienceDirect

Journal of Nuclear Materials

journal homepage: www.elsevier.com/locate/jnucmat

Oxidation of 316L(N) stainless steel in liquid sodium at 650 °C

Matthieu Rivollier [a, b], Jean-Louis Courouau [a, *], Michel Tabarant [c], Cécile Blanc [c], Marie-Laurence Giorgi [b]

[a] Den-Service de la Corrosion et du Comportement des Matériaux dans leur Environnement (SCCME), CEA, Université Paris-Saclay, F-91191, Gif-sur-Yvette, France
[b] CentraleSupélec, Université Paris-Saclay, Laboratoire de Génie des Procédés et Matériaux, 3 rue Joliot-Curie, F-91192 Gif-sur-Yvette cedex, France
[c] Den- Service d'Études Analytiques et de Réactivité des Surfaces (SEARS), CEA, Université Paris-Saclay, F-91191, Gif-sur-Yvette, France

HIGHLIGHTS

- Austenitic steel is immersed in liquid sodium containing oxygen at 650 °C until 500 h.
- $NaCrO_2$ is formed. O and Na come from liquid metal, Cr from steel.
- Mo and Fe rich M_6C carbides are formed. Mo and Fe come from steel, C from liquid metal.
- Cavities are also observed. They are due to oxidation, carburization and dissolution.
- Cr depletion is observed nearby the surface and in the vicinity of grain boundaries.

GRAPHICAL ABSTRACT

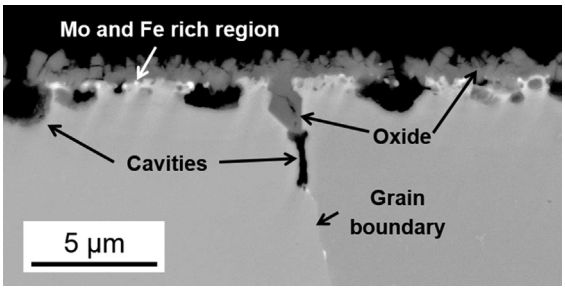

ARTICLE INFO

Article history:
Received 19 September 2017
Received in revised form
5 December 2017
Accepted 24 December 2017
Available online 28 December 2017

Keywords:
Liquid sodium
Austenitic steel
High temperature corrosion
Selective oxidation

ABSTRACT

The corrosion of an austenitic steel in liquid sodium containing 189 µg g^{-1} of oxygen was investigated at 650 °C as a function of time (122, 250 and 500 h). The steel samples were characterized by means of complementary techniques, namely scanning electron microscopy, X-ray diffraction, glow discharge optical emission spectroscopy and transmission electron microscopy. The characterizations showed that a $NaCrO_2$ oxide scale forms at the steel surface. Under this oxide scale, iron and molybdenum rich M_6C carbide particles together with $NaCrO_2$ in the grain boundaries and cavities filled with sodium were observed. The stainless steel substrate and/or the chromite scale were dissolved in parallel with the formation of chromite and carbides. Thermodynamic calculations showed that $NaCrO_2$ and M_6C are equilibrium phases in such a system. $NaCrO_2$ is formed by the reaction of chromium diffusing from the steel bulk with sodium and dissolved oxygen (external selective oxidation). Mo segregates to the steel surface where it reacts with Fe from the steel and C dissolved in liquid sodium. The dissolution of stainless steel occurred since the liquid sodium bath is not saturated in the dissolving species (pure metals and oxides such as $NaCrO_2$, Na_4FeO_3). As for the cavities, vacancies are created at the steel/$NaCrO_2$ interface by Cr oxidation, carburization and dissolution of the other elements present in the stainless steel. The vacancies become supersaturated and this leads to the nucleation of the cavities observed. Part of the vacancies created by Cr oxidation or steel dissolution is annihilated at sinks like dislocations leading to the translation of the oxide/metal interface towards the metal bulk.

* Corresponding author.
E-mail addresses: matthieu.rivollier@centralesupelec.fr (M. Rivollier), jean-louis.courouau@cea.fr (J.-L. Courouau), michel.tabarant@cea.fr (M. Tabarant), cecile.blanc@cea.fr (C. Blanc), marie-laurence.giorgi@centralesupelec.fr (M.-L. Giorgi).

https://doi.org/10.1016/j.jnucmat.2017.12.037
0022-3115/

1. Introduction

France made plans to construct the fourth generation of nuclear reactor and chose the Sodium-Cooled Fast Reactor (SFR) as the technology to develop. The expected economically reasonable service life-time of a reactor is 60 years. In these reactors, liquid sodium Na is used as a coolant at high temperatures (400–550 °C for the liquid metal bulk and up to 650 °C at the hot spots of the fuel claddings) [1]. As the chemical conditions can change with time (normal, transient and incidental), any interactions between the liquid metal and the structural materials (made mainly of austenitic steels) must be well known, well understood and predicted to guarantee service life-time as well as resistance to incidental conditions.

In sodium-cooled fast reactors, the liquid metal oxygen content is maintained at a maximum of 10 $\mu g\,g^{-1}$ by means of purification systems, in order to prevent solid oxide from precipitating in the circulation loops and minimize corrosion of the structural materials. However, certain events such as air or water leaks could occur during the service life-time of the nuclear reactor, leading to a temporary increase in the dissolved oxygen content (15 $\mu g\,g^{-1}$ to 200 $\mu g\,g^{-1}$ for unexpected transient) [2].

For austenitic steels immersed in liquid sodium containing low oxygen levels (less than 10 $\mu g\,g^{-1}$) for a few hundred or thousand hours, the corrosion is mainly due to the preferential dissolution of nickel and, to a lesser extent, chromium and manganese. This preferential dissolution leads to the ferritization of the steel surface. The thickness of the ferrite layer formed is of the order of a few μm [3–8]. At longer immersion times, austenitic steels are dissolved homogeneously with a kinetic attributed to iron dissolution [3,4]. An increase in the oxygen content or in the temperature is reported to increase the dissolution rate [4,6,7,9]. This is explained by an increase of the iron solubility in sodium in presence of oxygen [10,11]. Kolster et al. [12] show that oxygen might also increase the preferential dissolution rate of chromium, due to the formation of a Na-Cr-O dissolved complex.

At higher oxygen contents in liquid sodium, i.e. more than 15 $\mu g\,g^{-1}$ [8,13], oxide scales rich in Na and Cr are formed on the surface of austenitic or ferritic/martensitic steels. This oxide is $Na_2O.Cr_2O_3$, also called sodium chromite $NaCrO_2$ [8,9,14–16]. An increase in the oxygen content or in the temperature is reported to increase the oxidation rate [13–15]. The $NaCrO_2$ formation causes Cr depletion in the steel under the oxide scale, for both ferritic/martensitic [15,17] and austenitic steels [15]. In this case, the steel grain boundaries can be enriched in Na and O [14].

A discontinuous phase rich in Mo can also be formed at the surface or subsurface of steels containing Mo immersed in liquid sodium [3]. This phase could be Fe_7Mo_6 or M_6C type carbides at temperatures higher than 650 °C, M being Cr, Mn, Fe, Ni or Mo (liquid sodium contains traces of C) [8]. For instance, Fe_4Mo_2C was detected as shown in Ref. [9].

Finally, it can be concluded from this literature review that the mechanisms involved in the corrosion of austenitic steels in liquid sodium are very complex and not yet fully understood [18]. In recent years, as the experiments using liquid Na are not easy to perform, there are few studies on the corrosion in liquid Na. The influence of immersion time and dissolved oxygen content is not studied precisely enough to be confident in the results that could be obtained at long immersion times. The primary goal of our study, therefore, is to gain a better understanding of the corrosion mechanisms involved in liquid sodium in controlled temperature and oxygen content conditions and to investigate further a key step in the corrosion process: Cr diffusion from the steel bulk to the steel surface. The work is divided into the following stages:

1) Immersion of the chosen austenitic steel in liquid Na containing 189 $\mu g\,g^{-1}$ of oxygen at 650 °C for different immersion times up to 500 h;
2) Characterization of the samples obtained to determine the nature and composition of the corrosion products and estimate the oxidation depth;
3) Measurement of chromium concentration profiles in the vicinity of grain boundaries;
4) Discussion on the key mechanisms explaining the corrosion of austenitic steels in liquid sodium.

2. Materials and corrosion conditions

2.1. Stainless steel and sodium

The substrate tested is an austenitic stainless steel 316L(N) (provided by Industeel France). The dimensions of the steel specimens were 30 mm long, 20 mm wide and 1.5 mm thick. A 1 mm diameter hole along thickness took place at 3 mm from edge in the middle of the width. Its composition is given in Table 1. The analysis was performed using induced coupled plasma atomic spectroscopy and glow discharge optical emission spectroscopy for carbon. The grain size is close to 41 ± 2 μm (Fig. 1). Before the corrosion experiments, the specimens were polished in several stages. In order to study the influence of the steel surface roughness on corrosion in liquid sodium, it was decided to stop the mechanical polishing at different stages (1200 and 4000 grit SiC paper and 1 μm diamond suspension). The surface roughness obtained with this procedure was found to have a negligible influence on corrosion in liquid sodium during our trials (average roughness $Ra < 0.1$ μm). Therefore, the sample surface roughness is not given for the results described below.

High purity sodium (99.95 wt.%) was provided by Métaux Spéciaux SA. The principal impurities are $[Ca] < 2\,\mu g\,g^{-1}$, $[Cl] = 4\,\mu g\,g^{-1}$, $[Fe] = 1\,\mu g\,g^{-1}$, $[K] = 4\,\mu g\,g^{-1}$. It also contains traces of C. The quantitative analysis of carbon was not possible in our conditions due to contamination during analysis procedure. However, the experimental conditions of the test were already observed as carburizing for this low carbon steel [18]. The as-received solid sodium is covered with a sodium oxide layer, which is manually removed inside an argon-atmosphere glovebox.

2.2. Experimental conditions

The corrosion tests were run in a static sodium device called CorroNa [2]. The sodium (2.3 kg) is contained in a molybdenum crucible (MLR grade containing 0.7 wt.% of La_2O_3, Plansee), placed in a resistance heated furnace. Molybdenum dissolution in sodium was reported to be negligible in molybdenum-made circuit [12]. The device is set in a purified argon atmosphere (provided by Messer with a purity index 6.0, i.e. less than 3 vpm of H_2O and 2 vpm of oxygen and purified by zeolite adsorption), inside a glove box to simplify all operations involving preparing the test and handling the liquid metal. During the corrosion tests, the system containing the liquid sodium in contact with pure argon is perfectly sealed off from the argon atmosphere in the glove box.

After sodium melting, solid sodium oxides float to the free surface of the liquid metal, probably due to surface tension effects, allowing a first skimming operation to be performed to remove these sodium oxides. The liquid metal is then held at low temperature (105–110 °C) for 3 days. The new floating oxide is then carefully skimmed off from the free surface. An additional purification step is then performed at a high temperature (650 °C for

Table 1
Composition in wt.% of the 316L(N) stainless steel tested.

Fe	Cr	Ni	Mo	Mn	C	Si	P	S	Ti	Al	Cu	Co
Balanced	17.9	12.1	2.35	1.72	0.012	0.45	0.034	0.025	0.0015	0.0025	0.0025	0.0008

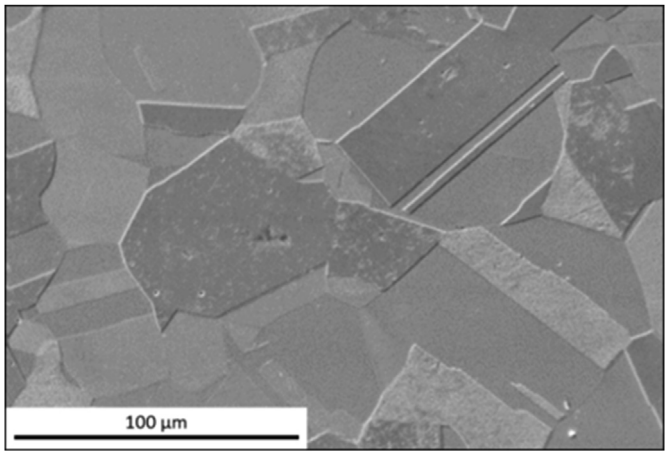

Fig. 1. 316L(N) steel microstructure after electrochemical etching (oxalic acid, 10 vol.%, 0.5 A cm^{-2}).

72 h), using a zirconium getter immersed in the liquid bath to eliminate any residual oxide and dissolved oxygen. The estimated dissolved oxygen content obtained after this purification step is 1 µg g^{-1} at the most. The dissolved zirconium concentration is known to be very low. For instance, at 722 °C, the zirconium solubility in sodium is 0.09 µg g^{-1} [19].

After purification, the liquid sodium bath is cooled to 120 °C and the zirconium getter is removed. Sodium oxide powder (Na_2O + 14.1 wt.% Na_2O_2, provided by Alfa Aesar) is added to the liquid sodium in order to obtain an oxygen concentration of 189 ± 8 µg g^{-1} (assuming that the initial oxygen concentration in the liquid sodium is equal to zero and that Na_2O and Na_2O_2 are completely dissolved in the liquid Na).

After this step, in order to keep the oxygen content of the sodium constant, the specimens are immersed in the molten sodium bath at 120 °C and the system is tightly closed. The sodium is then heated to 650 °C at a rate of 0.5 °C/min. The temperature is kept constant for 122 h, 250 h and 500 h before being decreased at a rate of 0.5 °C/min. The specimens are removed from the liquid sodium at 120 °C. The sodium residues present on the specimens are removed with 99.9 wt.% pure ethanol (provided by Carlo Erba) at ambient temperature. This soft cleaning procedure was chosen to remove the sodium residues from the surface and to keep as much as possible liquid sodium that might have penetrated into the corrosion surface layer during the corrosion processes.

2.3. Characterization techniques

Specimens are weighted before and after the corrosion test, using an AT20 weighing scale constructed by MettlerToledo. X-Ray Diffraction (XRD, Bruker D8 discover) was carried out to characterize the phases formed during corrosion. XRD was performed in the θ-2θ configuration with a copper cathode emitting X-rays of wavelength λ = 1.5406 Å. Characterizations were performed by means of Scanning Electron Microscopy (SEM, Zeiss LEO 1460VP) associated with Energy Dispersive X-ray spectroscopy (EDX, SAMX DXP-X10P), to observe and analyse the surfaces and polished cross-sections of the specimens. Elementary depth profiles were obtained from the sample surface using Glow Discharge Optical Emission Spectroscopy (GDOES). The instrument used was a GD-Profiler 2 from the Horiba Scientific company. The glow discharge was powered by a 13.56 MHz radio-frequency generator. A 4 mm-diameter copper anode and 99.9999 vol.% purity argon gas were used to sputter the sample (800 Pa and 30 W). The emission responses from the excited sputtered elements (O, Fe, Cr, Ni, Mo, C, Si, Mn, etc.) were detected using a polychromator with a focal length of 500 mm. A monochromator was used to determine the sodium concentration. The calibration curves used to quantify the metal elements were obtained by using bulk reference materials. The resulting depth in the reference materials was measured with a perthometer (PerthoConcept, Mahr Mesure). The crater depth cartography in the stainless steel was measured using an optical interferometer (Bruker ContourGT). A sample is also observed by Transmission Electron Microscopy (TEM), coupled with an EDX detector. The instruments used are a Tecnai Osiris TEM and a ChemiSTEM EDX detector, contructed both by FEI. The TEM characterizations are performed on a sample prepared by Focused Ion Beam (FIB) on a Strata 400S FIB, constructed by FEI.

Three specimens are obtained after 122 h, six after 250 h and three after 500 h in the CorroNa static sodium device. All the specimens are weighed before and after the corrosion test and further characterized by GDOES. All the samples obtained after 250 and 500 h are observed by SEM and analysed by EDX and DRX. One sample, immersed during 250 h is prepared by FIB and observed by TEM.

3. Experimental results highlighting corrosion processes

Fig. 2 gives the difference between the sample masses after and before immersion in liquid sodium (positive in case of mass gain and negative in case of mass loss) versus time. The formation of a solid product with impurities and/or sodium leads to a mass gain of the sample while a dissolution phenomena leads to a mass loss. In the test presented here, the sample mass increases after immersion in liquid sodium containing 189 µg g^{-1} of oxygen during 122 h. At longer immersion time, the sample loses mass when the immersion time increases.

3.1. Morphology and composition of the corrosion products

The surface of a sample immersed during 250 h is shown in Fig. 3a. The surface features are typical of the characterizations obtained in all conditions. Two morphologies are shown on the sample surface, a dark one and a grey light one.

The sample surface is mainly covered with triangle-shaped crystals, rich in chromium, sodium and oxygen (Fig. 3b, EDX analysis of the white cross in Fig. 3a). Iron, nickel and molybdenum are also detected in this area, probably from the steel substrate. Considering the triangle shape [8] combined with the elements detected by EDX and thermodynamic data [20], this phase might be sodium chromite $NaCrO_2$.

The clearer phase is rich in molybdenum and iron (Fig. 3c, EDX analysis of the black cross in Fig. 3a). Chromium and nickel are also detected in this phase, probably from the steel substrate.

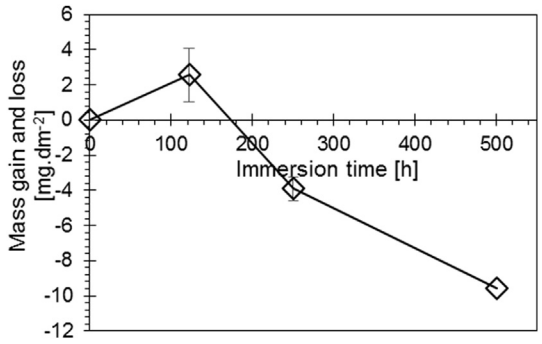

Fig. 2. Mass gain or loss of samples immersed at 650 °C in liquid sodium containing an oxygen content of 189 μg g^{-1} as a function of time.

3.2. Nature of the phases formed during corrosion

The different phases described in Section 3.1 were characterized using XRD to determine their chemical nature. The experimental XRD diagram, obtained for the steel sample immersed in liquid sodium at 650 °C for 500 h, was compared with the theoretical diagram of austenite, $NaCrO_2$ and several M_6C carbides containing Cr, Mn, Fe, Ni and Mo (Fig. 4). The XRD characterizations confirmed the formation of both sodium chromite ($NaCrO_2$) and M_6C carbides for all the corrosion times. The closer carbide seems to be Fe_3Mo_3C. These characterizations confirm the formation of sodium chromite previously characterized by SEM [13] and clarify the nature of the molybdenum rich phase as M_6C, a molybdenum and iron rich carbide.

3.3. In-depth corrosion

3.3.1. Cross-section observations

The cross-section of a sample immersed in liquid sodium for 250 h at 650 °C is shown in Fig. 5. This SEM image is obtained in backscattered electron (BSE) mode, in which materials with elements composed of higher atomic number (Z) appear clearer than the one with lower Z elements.

At the top of the image, the mounting resin appears in black. At the bottom, the stainless steel appears to be grey. A dark grey layer, corresponding to the sodium chromite layer, is observed below the mounting resin. This sodium chromite layer seems to be discontinuous in some locations. In between this oxide scale and the steel substrate, cavities (dark areas) are formed. In addition, a lighter grey phase is seen between the Cr-Na-O-rich zone and the top of the cavity zone. This phase might be molybdenum and iron rich carbide M_6C.

A grain boundary is visible in the middle of the cross-section. This grain boundary emerges at the steel surface and was probably in contact with liquid sodium at the beginning of the corrosion process. Its upper part is filled with oxide. A cavity is present immediately beneath oxide.

3.3.2. In-depth concentration profiles

The composition depth profiles of carbon, oxygen, chromium, iron, nickel, molybdenum and sodium obtained through GDOES are plotted together in Fig. 6. The element compositions in log-scale are given as a function of depth for the sample corroded for 250 h at 650 °C in liquid sodium with an oxygen content of 189 μg g^{-1}. The origin of the *x*-axis corresponds to the specimen surface. The maximum depth of 12 μm corresponds to the mean depth of the crater left by the analysis. The scales of the two analyses (GDOES, Fig. 6 and SEM, Fig. 5) are not an exact match: 5 μm in the SEM image corresponds to 4 μm in the composition depth profile. This slight difference can be explained by the fact that the composition profiles measured through GDOES are averaged over the 4 mm-diameter area analysed, whereas SEM provides a much more local observation and by the fact that the erosion rate might be slightly different from one phase to the other. In any case, as is shown

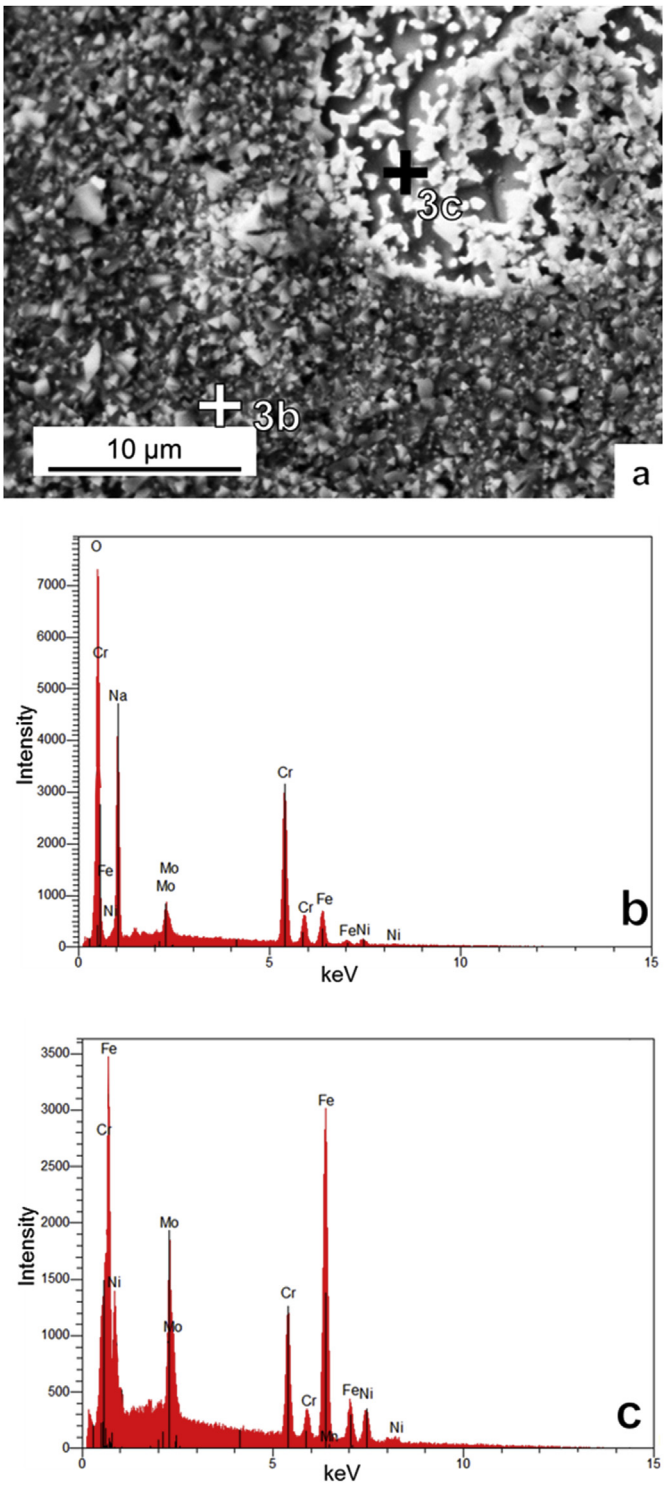

Fig. 3. Sample immersed for 250 h at 650 °C in liquid sodium containing an oxygen content of 189 μg g^{-1}, a) SEM observation in secondary electrons at 2 kV and associated b) and c) EDS spectra); The steel surface is covered with a layer of triangle-shaped crystals rich in Na, Cr and O. Mo and Fe rich particles are also detected.

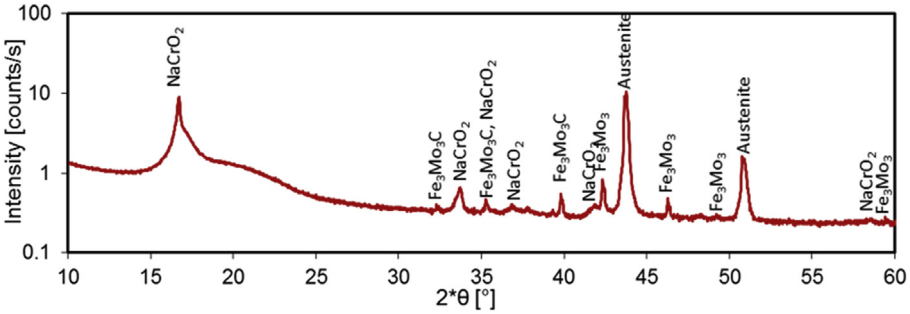

Fig. 4. XRD diagram, specimen immersed for 500 h at 650 °C in liquid sodium containing 189 μg g^{-1} oxygen. $NaCrO_2$ and Fe_3Mo_3C are identified together with the austenite substrate.

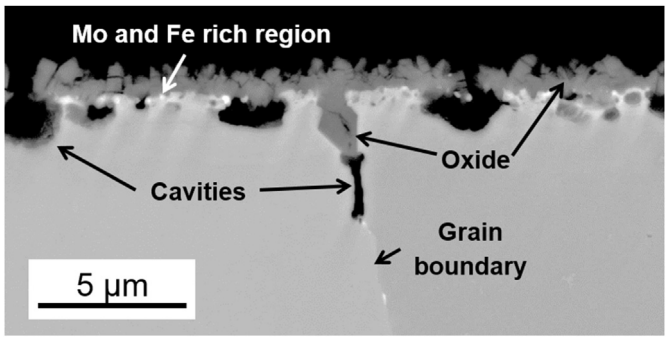

Fig. 5. SEM cross-section observations (backscattered electrons); sample immersed for 250 h at 650 °C in liquid sodium with a 189 μg g^{-1} oxygen content.

below, the agreement between the two characterizations is excellent. The different depths cited below are deduced from the GDOES profiles.

At the steel surface, the composition profiles indicate enrichment in oxygen, sodium and chromium in a 1 μm-thick surface layer, corresponding to the sodium chromite scale (Figs. 4 and 5). It should be noted that the oxygen composition decreases whereas the sodium and chromium compositions slightly increases in this oxide scale from the surface to the depth of 1 μm. The iron, nickel and molybdenum compositions increase in the oxide scale from nearly 0.1 at.% at the specimen surface to 8, 2 and 2 at.% respectively.

The composition profiles under the oxide scale differ from those of the bulk of the steel substrate. The thus affected area corresponds to the presence of corrosion products (Figs. 4 and 5) and can be divided into two zones. The first zone is located at depths between 1 μm and 1.55 μm beneath the specimen surface. The compositions of molybdenum and carbon rise to a peak of 3.1 at.% and 0.38 at.% respectively at approximately 1.3 μm. These composition peaks correspond to the Mo and Fe-rich carbides (light grey phase, Fig. 5). The Cr composition profile presents a slightly depleted zone at around 1.55 μm. The evolution as a function of immersion time (less than 500 h) of the location of the chromium minimum concentration could not be measured because included in the measurement uncertainty (±0.2 μm). The second zone is located at depths ranging between 1.55 and 5.25 μm, with a slight increase in the Fe, Cr and Ni compositions to their bulk values and a sharp decrease in the C, O and Na contents. The slope changes in the sodium composition profile (inflexion points indicated by arrows in Fig. 6) are consistent with the characteristic depth of internal oxides and cavities formed underneath at the grain boundaries.

Under the affected area, no corrosion products are found in the steel substrate (Fig. 5). However, the Na and O contents are not equal to zero and they decrease slightly to their detection limits. This last segment of the composition profiles, plotted in Log-scale, must be considered with care and could be an artefact of the GDOES measurements because the shape of the sputter crater shows a steadily increasing deviation from its ideal shape upon increasing sputtering time. Additionally, crater edge effects provide a more significant contribution to the overall signal upon increasing crater depth.

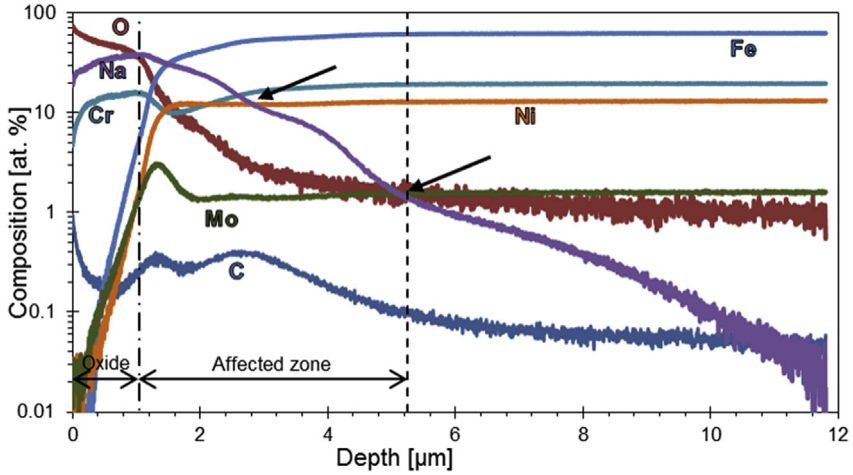

Fig. 6. GDOES chemical depth profiles obtained for a sample immersed in liquid sodium for 250 h at 650 °C with an oxygen content of 189 μg g^{-1}.

In the end, it should be reminded that the experimental results described above were obtained for different surface roughnesses, obtained by mechanical polishing stopped at different stages (1200 and 4000-grit SiC paper and 1 μm diamond suspension). Our tests demonstrated that the corresponding surface roughnesses have no influence on the corrosion mechanisms studied.

4. Chromium concentration evolution nearby the surface

In the literature, it is demonstrated that oxygen strongly affects the behaviour of chromium by the formation of $NaCrO_2$ [13–17]. That is why the evolution of chromium concentration was analysed close to metallurgical defects such as grain boundaries (section 4.1). The mean chromium concentration was also characterized as a function of immersion time (section 4.2).

4.1. Evolution of chromium concentration along an emerging grain boundary

Thin foils obtained by FIB are useful to measure the local elementary composition by EDX with TEM. This experimental technique is used to characterize chromium composition around a grain boundary.

The HAADF (High-Angle Annular Dark-Field) image of a sample immersed during 250 h in liquid sodium containing 189 $\mu g\, g^{-1}$ of oxygen at 650 °C is presented in Fig. 7. The white layer at the top of the image corresponds to a tungsten protecting layer deposited during FIB processing. The dark grey layer below corresponds to the sodium chromite layer. The steel grain boundary is highlighted by a dotted line. Some white spots, corresponding to M_6C carbides, are visible between the metal and the sodium chromite layer. Cavities are not present on this part of the sample.

The red arrows numbered "1" and "2" in Fig. 7 correspond to the location of the chromium EDX analysis shown in Fig. 8. The chromium concentration is plotted as a function of distance from the grain boundary (located at abscissa 0). The measurement length was 100 nm in the left steel grain and 350 nm in the right steel grain. The chromium composition decreases from the center of the grains to the grain boundary where it reaches a minimum. The concentration profile 1 exhibits two Cr concentration peaks which might correspond to small phases rich in chromium such as carbides or oxides.

Moreover, the chromium concentration of profile 1 is lower than the concentration of profile 2, because the location of profile 1 is closer to the surface.

To summarize, the alloy is chromium-depleted around emerging grain boundary, and closer the location is to the steel surface and the grain boundary, higher the chromium depletion is.

4.2. Evolution of chromium depletion as a function of immersion time

The mean chromium concentration profile measured by GDOES is given as a function of depth in Fig. 9 for three immersion times in liquid sodium (122, 250 and 500 h). For all trials, the origin of *x*-axis is placed at the minimum chromium concentration, assumed to be the interface between steel and corrosion products as discussed before (section 3.3.2). At 10 μm depth at the most, the Cr concentration of all samples reaches the initial concentration of the studied steel for the three immersion times. In the following, this steel zone that is not affected by corrosion is called the steel bulk.

At the interface between steel and corrosion products, the chromium concentration does not depend on immersion time. From this interface to the bulk, the chromium concentration increases in all cases. The lower chromium concentration is obtained

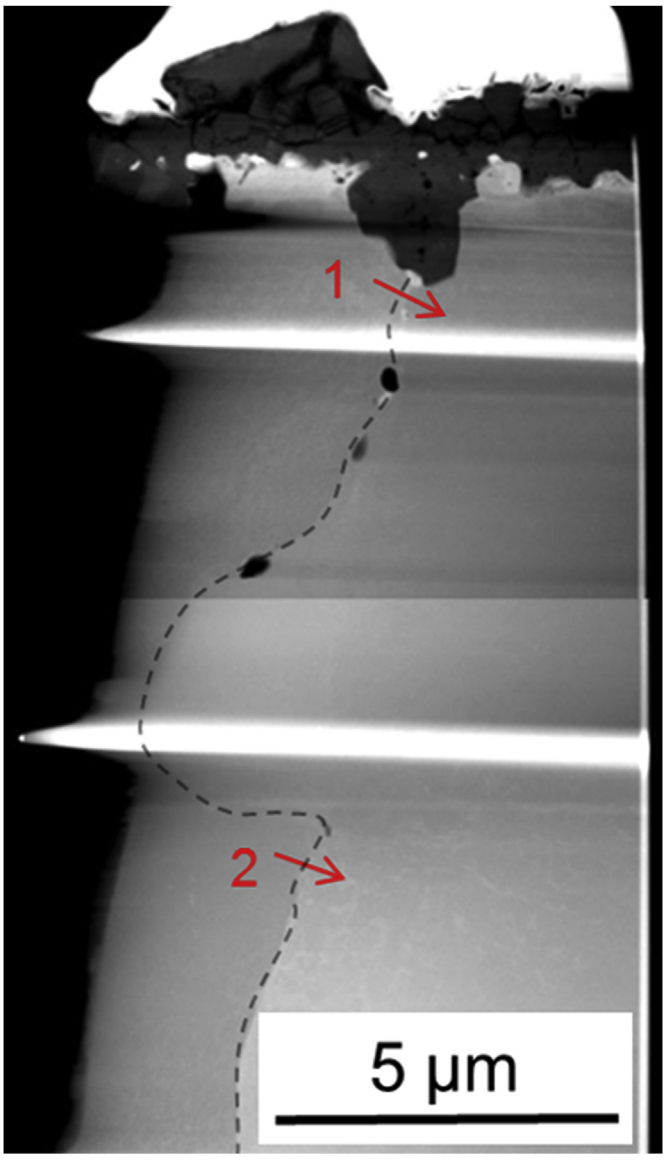

Fig. 7. Cross section of a sample immersed for 250 h at 650 °C in liquid sodium with 189 $\mu g\, g^{-1}$ of oxygen (HAADF image). The $NaCrO_2$ scale is visible at the top of the image in black.

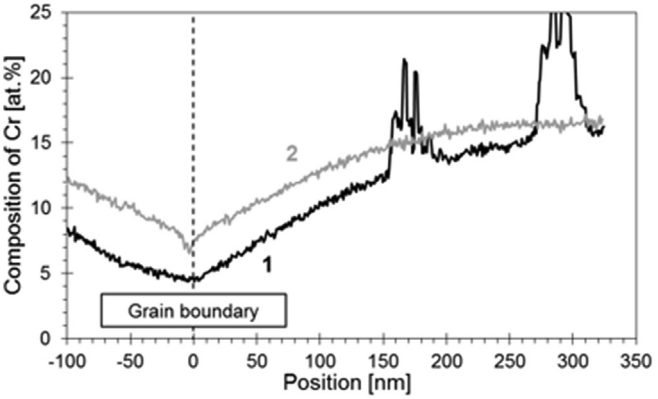

Fig. 8. Chromium composition profile obtained by EDX analysis at the locations shown by arrows 1 and 2 in Fig. 7. Abscissa 0 corresponds to the location of the grain boundary where a chromium depletion is observed.

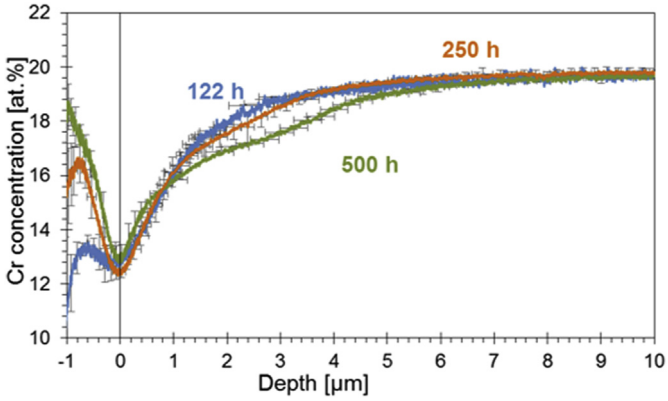

Fig. 9. Chromium composition profile obtained by GDOES analysis for samples immersed during 122, 250 and 500 h at 650 °C in liquid sodium containing 189 µg g^{-1} of oxygen.

for the samples immersed longer in liquid sodium. The samples immersed during 500 h are more chromium depleted than the samples immersed during 250 h which are also more depleted than the samples immersed during 122 h.

5. Discussion

In the following sections, a discussion is held concerning the final structure of the corrosion products (Section 5.1) and the mechanisms explaining their formation (Section 5.2).

5.1. Final structure of the corrosion products

As shown in Section 3, during immersion in liquid sodium containing 189 µg g^{-1} of oxygen at 650 °C, the stainless steel studied became covered with a sodium chromite ($NaCrO_2$) layer. Molybdenum and iron rich carbides (M_6C) are also formed underneath. These observations confirm previous results described in the literature, i.e. formation of sodium chromite [8,12–16] and carbides [9] in oxidizing and carburizing conditions.

The system studied here is composed of liquid sodium containing traces of dissolved oxygen and carbon in contact with a stainless steel containing Cr, Fe and Mo. Thermodynamic calculations described below will show that $NaCrO_2$ and M_6C are equilibrium phases in such a system.

5.1.1. Oxides' stability

Three main solid oxides can be formed at the steel surface or in liquid sodium: sodium chromite ($NaCrO_2$), sodium ferrate (Na_4FeO_3) [21] and sodium oxide (Na_2O).

At the steel surface, the chemical reaction corresponding to solid Na_xMO_y formation can be written as follows:

$$[O] + \frac{x}{y}\cdot Na_{liq} + \frac{1}{y}.M_{steel} \rightarrow \frac{1}{y}Na_xMO_y \quad (1)$$

where M_{steel} = Fe or Cr in solid solution in steel, x and y are the stoichiometric coefficients of Na_xMO_y and [O] corresponds to oxygen dissolved in liquid sodium.

The reference state is chosen to be pure liquid sodium, pure body-centered cubic solid M and pure O_2 at standard pressure of 1.013 bar. At thermodynamic equilibrium, the law of mass action is given by:

$$\mu_{[O]} = \frac{1}{y}\cdot\left(\Delta G^0_{f,Na_xMO_y} + RT\cdot\ln\frac{a_{Na_xMO_y}}{a_M.a_{Na}}\right) \quad (2)$$

where $\mu_{[O]}$ is the chemical potential of oxygen in liquid sodium, $\Delta G^0_{f,Na_xMO_y}$ is the standard Gibbs free energy of formation of Na_xMO_y, R is the gas constant ($R = 8.314$ J mol^{-1} K^{-1}), T is the temperature, $a_{Na_xMO_y}$, a_M and a_{Na} are the activities of Na_xMO_y, M and Na respectively.

As a first approximation, liquid sodium and the oxides formed can be considered to be pure, i.e., $a_{Na} = 1$ and $a_{Na_xMO_y} = 1$. The activities of Fe and Cr in austenite are calculated as a function of temperature by means of the CALPHAD method implemented in ThermoCalc®, with the TCFE8 (Steels/Fe-Alloys v8.0) database. For instance, at 650 °C, $a_{Fe} = 0.67$ and $a_{Cr} = 0.28$, in using the reference as pure stable metal (body-centered cubic for chromium and iron). The steel composition used for the calculation is limited to the main elements (Cr, Ni, Mo, Mn, C, Si and Fe). The contents of Cr, Ni, Mo, Mn, C and Si are the ones given in Table 1 and the balanced Fe content is slightly higher than in the real stainless steel. This choice was made because the calculation including the minor elements did not converge. With this choice, the activities of the chosen elements are supposed to be weakly dependent on minor elements. This seems quite reasonable for Cr and Fe which are the only ones considered for the oxides' formation ($NaCrO_2$ and Na_4FeO_3). The Cr and Fe contents are indeed much higher than those of the other elements. The standard Gibbs free energy of formation (in kJ.mol^{-1}) of $NaCrO_2$ ($-874.6 + 0.20921\ T$) and Na_4FeO_3 ($-1214.17 + 0.34269\ T$) are given in Ref. [20] as a function of temperature T in K. The relative stability of both oxides can be shown in the Ellingham diagram presented in Fig. 10a. The chemical potential of oxygen in liquid sodium given by Eq. (2) is plotted as a function of temperature for Na_4FeO_3 (purple line) and $NaCrO_2$ (blue line). The oxide is spontaneously formed in the region above the corresponding straight line.

In liquid sodium, the chemical reaction corresponding to solid Na_2O formation can be written as follows:

$$[O] + 2\cdot Na_{liq} \rightarrow Na_2O \quad (3)$$

At thermodynamic equilibrium, the law of mass action leads to:

$$\mu_{[O]} = \Delta G^0_{f,Na_2O} + RT\cdot\ln\frac{a_{Na_2O}}{a_{Na}} \quad (4)$$

where $\Delta G^0_{f,Na_2O}$ (=-421.5 + 0.1414 T in kJ.mol^{-1} [22]) is the standard Gibbs free energy of formation of Na_2O and $a_{Na} = 1$. If Na_2O is supposed to be pure, $a_{Na_2O} = 1$. In this case, the chemical potential of oxygen in liquid sodium given by Eq. (4) is represented by the black straight line in the Ellingham diagram (Fig. 10a). Na_2O is spontaneously formed in the region above this straight line.

The chemical potential of oxygen in liquid sodium must be calculated in the conditions studied here (i.e., [O] = 189 µg g^{-1} and 650 °C), in order to determine if the oxides considered above (Na_4FeO_3, $NaCrO_2$ and Na_2O) are stable.

$$\mu_{[O]} = R.T.\ln a_{[O]} \quad (5)$$

where $a_{[O]}$ is the activity of oxygen in liquid sodium, the reference state being pure O_2 at standard pressure of 1.013 bar. The solubility of oxygen in sodium $w^{Na,sat}_{[O]}$ can be found in the literature [23] ($\log w^{Na,sat}_{[O]} = 6.2571 - \frac{2444.5}{T}$ in µg.g^{-1}). It can therefore be convenient to define the activity of oxygen in liquid sodium $a'_{[O]}$ with the

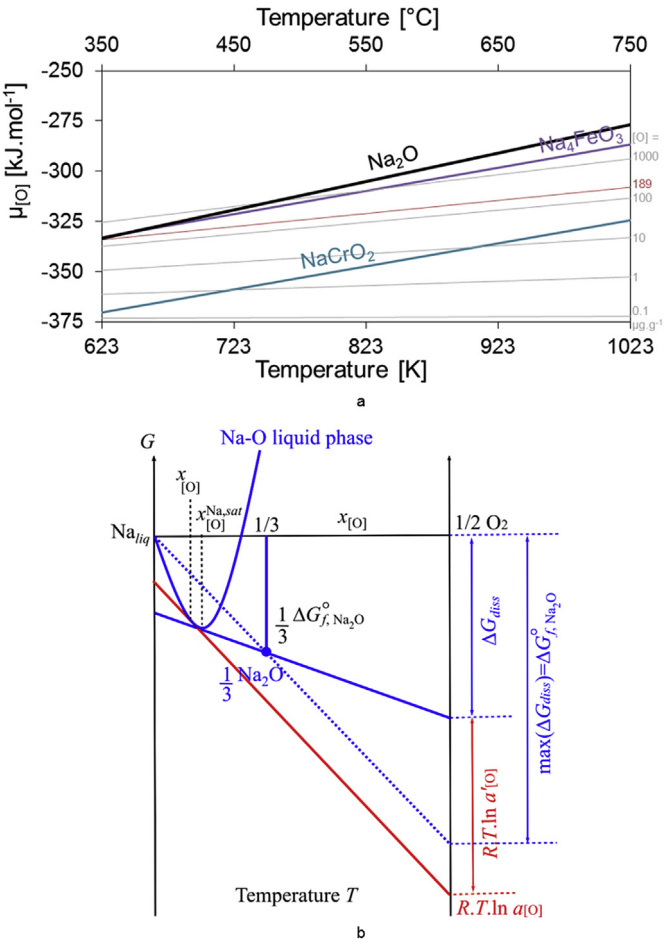

Fig. 10. Oxides' stability: a) Ellingham diagram of $NaCrO_2$, Na_4FeO_3 and Na_2O plotted together with the chemical potential of oxygen for different oxygen contents in liquid sodium; b) Gibbs free energy diagram for the equilibrium between Na-O liquid phase and Na_2O.

reference state of liquid sodium saturated in oxygen (i.e., $a'_{[O]} = 1$ for oxygen-saturated liquid sodium).

Oxygen is present in small quantities in liquid sodium, in the form of a dilute solution (at 650 °C, $w^{Na,sat}_{[O]} = 0.4$ wt.% or $x^{Na,sat}_{[O]} = 0.6$ mol.%). As currently done for oxygen in liquid iron [24], Henry's law can be used to express the activity of oxygen in liquid sodium:

$$a'_{[O]} = \gamma^{\circ}_{[O]} \cdot x_{[O]} \tag{6}$$

where $\gamma^{\circ}_{[O]}$ is the Henry's law constant and $x_{[O]}$ the mole fraction of oxygen in liquid sodium. Assuming that Henry's law is validated for oxygen content lower than or equal to its solubility in liquid sodium:

$$\gamma^{\circ}_{[O]} = \frac{1}{x^{Na,sat}_{[O]}} \tag{7}$$

and

$$a'_{[O]} = \frac{x_{[O]}}{x^{Na,sat}_{[O]}} \tag{8}$$

As the oxygen content is low in liquid sodium, the activity of oxygen is also given by:

$$a'_{[O]} = \frac{w_{[O]}}{w^{Na,sat}_{[O]}} \tag{9}$$

Finally,

$$\mu_{[O]} = R.T.\ln a_{[O]} = R.T.\ln a'_{[O]} + \Delta G_{diss} \tag{10}$$

where ΔG_{diss} is the Gibbs free energy change for the chemical reaction

$$\frac{1}{2}O_{2\,(gas)} \rightarrow [O]^{sat}_{Na_{liq}} \tag{11}$$

with $[O]^{sat}_{Na_{liq}}$ the oxygen dissolved in liquid sodium at saturation.

To our knowledge, there is no measurement of ΔG_{diss} in the literature. Fig. 10b represents the Gibbs free energy of formation of Na-O binary phases as a function of mole fraction of oxygen $x_{[O]}$ at a particular temperature T, the reference state being pure liquid sodium and pure O_2 gas. The general case is schematized in blue. The Gibbs free energy of formation of Na-O liquid phase is represented by the blue curve. The coordinates of the point corresponding to Na_2O are $x_{[O]} = \frac{1}{3}$ and $\frac{1}{3}.\Delta G^0_{f,Na_2O}$. When Na_2O is in equilibrium with the liquid phase, the point corresponding to Na_2O belongs to the straight line tangent to the liquid phase curve at the composition $x^{Na,sat}_{[O]}$. This tangent line cuts the $x_{[O]} = 1$ axis at the ordinate $R.T.\ln a^{Na,sat}_{[O]}$, where $a^{Na,sat}_{[O]}$ is the activity of oxygen in liquid sodium in equilibrium with Na_2O. This intersect also corresponds to the origin of the $a'_{[O]}$ scale (i.e., $R.T.\ln a'_{[O]} = 0$, Eq. (8)). The corresponding ΔG_{diss} is then given by Eq. (10) written in this particular case:

$$\mu_{[O]} = R.T.\ln a^{Na,sat}_{[O]} = \Delta G_{diss} \tag{12}$$

If the oxygen content $x_{[O]}$ in liquid Na is less than $x^{Na,sat}_{[O]}$, the red tangent line (Fig. 10b) to the liquid phase curve cuts the $x_{[O]} = 1$ axis at the ordinate $R.T.\ln a_{[O]}$. The different terms of Eq. (10), in particular $R.T.\ln a'_{[O]}$, can be determined as shown in Fig. 10b.

The value of ΔG_{diss} depends on the shape of the Gibbs free energy of formation of Na-O liquid phase which is unknown. As oxygen is dissolved in liquid Na, $\Delta G_{diss} \leq 0$. Another limiting case is presented in Fig. 10b, with the blue dashed line. It corresponds to the mimimum value of the Gibbs free energy of formation of Na-O liquid phase at $x^{Na,sat}_{[O]}$ and therefore the maximum value of ΔG_{diss}. Using Thales' theorem,

$$\Delta G_{diss} > \Delta G^0_{f,Na_2O} \tag{13}$$

Finally, with the real shape of the Gibbs free energy of formation of Na-O liquid phase,

$$\Delta G^0_{f,Na_2O} < \Delta G_{diss} < 0 \tag{14}$$

At 650 °C, $-290988 < \Delta G_{diss} < 0$ (J mol^{-1}).

As liquid sodium is almost pure, the activity of Na in liquid sodium can be expressed by Raoult's law. With this assumption, the solid blue line described above cuts the $x_{[O]} = 0$ axis at the ordinate $R.T.\ln(1 - x^{Na,sat}_{[O]})$ and the $x_{[O]} = 1$ axis at the ordinate given by:

$$\mu_{[O]} = \Delta G^0_{f,Na_2O} - 2\,R.T.\ln\left(1 - x^{Na,sat}_{[O]}\right) = \Delta G_{diss} \tag{15}$$

For instance, at 650 °C, the solid blue line cuts the $x_{[O]} = 0$ (resp. $x_{[O]} = 1$) axis at -45 J mol^{-1} (resp. -290898 J mol^{-1}). Finally, ΔG_{diss}

can be estimated by $\Delta G^0_{f,Na_2O}$ since the relative uncertainty induced by this approximation is less than 0.05% in the temperature range [400; 700 °C]. This means that the tangent line to the liquid phase curve at the composition $x^{Na,sat}_{[O]}$ is close to the blue dashed line.

In Fig. 10a, $\mu_{[O]} = R.T.\ln a_{[O]}$ (Eq. (10)) is plotted for different oxygen contents in liquid sodium and $\Delta G_{diss} = \Delta G^0_{f,Na_2O}$. Let us first consider the curve corresponding to an oxygen content of 1000 μg g^{-1}. The calculation predicts that solid Na_2O is in equilibrium with liquid sodium containing 1000 μg g^{-1} for temperatures less than 751 K. This is in good agreement with measurements found in the literature [23]. This means that the unknown value ΔG_{diss} can be approximated by $\Delta G^0_{f,Na_2O}$ (as was done before [21]). For an oxygen concentration of 189 μg g^{-1} in liquid sodium (red $\mu_{[O]}$ curve, Fig. 10a), at temperatures higher than 350 °C, the chemical potential of oxygen is lower than the one required to form Na_2O or Na_4FeO_3 and higher than the one required to form $NaCrO_2$. It implies that in our experimental conditions, i.e., 650 °C and 189 μg g^{-1} of oxygen, the sodium chromite formation is thermodynamically possible while the formation of sodium oxide and sodium ferrate is not possible.

5.1.2. Carbides' stability

The carbides' stability is also investigated by means of ThermoCalc® based on CALPHAD method, with the TCFE8 (Steels/Fe-Alloys v8.0) database. As for the calculations of the oxides' stability, the steel composition is limited to the main elements in austenite (Cr, Ni, Mo, Mn, C, Si with the contents given in Table 1 and Fe with a content slightly higher than in the real stainless steel). The carbides considered are $M_{23}C_6$, M_3C_2, M_5C_2, M_6C, M_7C_3, where M can be Cr, Mn, Fe, Ni and Mo. The activity of the elements in austenite in equilibrium with carbides is essentially unchanged (lower than 1 hundredth) compared to the activity of the elements in austenite (used in section 5.1.1).

Fig. 11a gives the results of the mole fraction of stable phases as a function of temperature. The mole fraction of austenite is closed to 1 for all temperatures. The most stable carbide is M_6C for temperatures below 615 °C ($M_{23}C_6$ also exists but at a very low molar fraction less than 10^{-3}) and $M_{23}C_6$ for temperatures higher than 650 °C (together with M_6C at a very low molar fraction). In between, both carbides are present. Fig. 11b and c present the elemental composition of M_6C and $M_{23}C_6$ carbides. M_6C carbides contain mainly Mo, Fe and C and $M_{23}C_6$ carbides mainly Cr and C. At 650 °C, the carbides formed in the stainless steel studied here are rich in Mo and the XRD peaks are consistent with M_6C carbides containing mainly Mo, Fe and C (such as Fe_3Mo_3C) and in small proportions Cr, Mn and Ni. At 650 °C, the M_6C composition given by thermodynamic calculations is close to Mo_4Fe_2C (Fig. 11b) (Mo: 48 at.%, Fe: 29.3 at.%, C: 14.3 at.%, Cr: 8 at.%). It can therefore be concluded that the M_6C carbides formed are in thermodynamic equilibrium in the system, even if the calculated maximum temperature for M_6C stability is less than 650 °C (Fig. 11a). This temperature could be slightly underestimated by the calculations.

5.2. Mechanisms and driving forces of corrosion phenomena

Corrosion tests in liquid sodium containing 189 μg g^{-1} of oxygen at 650 °C pointed out the formation of corrosion products composed of sodium chromite $NaCrO_2$ and M_6C carbides containing Mo and Fe (Fig. 4). The observation of cross sections showed that cavities are formed between these corrosion products and the stainless steel (Fig. 5). Finally, a dissolution of the stainless steel is highlighted by the mass loss measured for immersion durations of 250 and 500 h (Fig. 2).

The oxidation and carburation mechanisms are described in Section 5.2.1, the dissolution driving forces in Section 5.2.2 and the cavities formation mechanisms in Section 5.2.3.

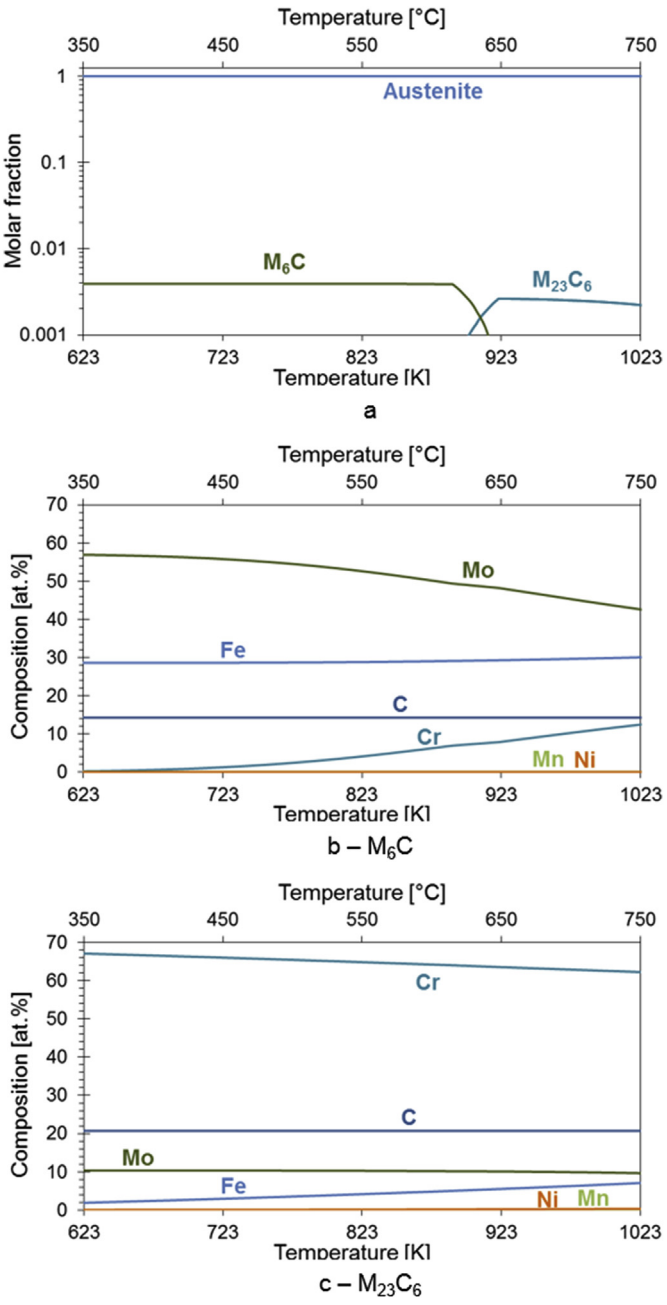

Fig. 11. Carbides'stability: a) mole fraction of stable phases, b) Composition of M_6C carbide as a function of temperature and c) Composition of $M_{23}C_6$ carbide as a function of temperature.

5.2.1. Oxidation and carburation mechanisms

5.2.1.1. Selective oxidation. The stainless steel surface under study became covered with a $NaCrO_2$ scale during immersion in liquid sodium. This is a selective oxidation phenomenon, chiefly external, i.e. it occurs on the stainless steel surface (Fig. 5). From a depth of 10 μm and moving towards the steel surface, the general shape of the chromium profiles exhibit an initial, constant concentration zone that corresponds to the concentration in the stainless steel bulk then a concentration decrease down to minimum concentration (depletion zone) and, finally, an increase in concentration towards the surface (Fig. 9). The concentration profiles obtained are

the result of Cr selective oxidation with Cr diffusion from the steel bulk to the $NaCrO_2$/steel interface (depth = 0, Fig. 9) and $NaCrO_2$ formation on the steel surface (depth < 1 μm, Fig. 9). The mimimum Cr concentration remains more or less constant at approximately 12 ± 1 at.% from 122 to 500 h (average and uncertainty on all specimen). This concentration could correspond to Cr concentration in the stainless steel at equilibrium with $NaCrO_2$. However, caution should be exercised with the conclusion about this particular issue, as a rough thermodynamic assessment would rather give a Cr concentration in equilibrium with $NaCrO_2$ close to the null value [28] and precise experimental data are still lacking. Indeed, it should be mentioned that the measurement of the Cr concentration by GDOES probably lacks of accuracy. This is a mean Cr concentration measured by sputtering the elements in a 4 mm diameter crater with the contribution of the different corrosion products. For instance, tiny carbides (Fig. 8) contribute as well to the Cr concentration.

In Fig. 9, the shape of Cr concentration profiles is characteristic of diffusion in polycrystalline materials [25–28], with the influence of the presence of grain boundaries (e.g., from 1.6 to 4.6 μm at 500 °C). This is confirmed by the Cr concentration profiles measured in the vicinity of grain boundaries (Fig. 8). Cr depletion is larger in the grain boundary than in the adjacent grains. This result indicates that the Cr diffusion coefficient is higher in the grain boundary than in the grain (grain boundaries are known to be diffusion short-circuits [32]). In Fig. 8, the local Cr concentration decreases from the steel bulk (profile 2) to the surface (profile 1). This is in good agreement with the mean Cr concentration profiles measured by GDOES as described just before.

Finally, $NaCrO_2$ is formed by the reaction of chromium diffusing from the steel bulk with two components of liquid metal, namely sodium and dissolved oxygen. The oxidation front can be located either at the $NaCrO_2$/steel interface or $NaCrO_2$/liquid metal interface. The experiments presented here do not show where the oxidation front is located. Some prior results at 550 °C are reported in the literature [28], indicating an inner oxidation front.

5.2.1.2. Carbides formation. M_6C carbides rich in Fe and Mo were present in between the $NaCrO_2$ scale and the stainless steel after immersion in liquid sodium (Fig. 5). Mo segregates to the steel surface where it reacts with Fe from the steel and dissolved C present in liquid sodium. The experimental conditions of the test were already observed as carburizing for this low carbon steel [18], probably because of high carbon content due to the fabrication process of the sodium metal. Carbon diffuses into the steel matrix and precipitates into carbides representative of the local composition: Mo rich carbide (peak at 1.5 μm in Fig. 6), or Fe-Cr rich carbides (peak at 2.8 μm in Fig. 6). The Mo concentration profiles obtained present a slight depletion zone (around 2 μm in Fig. 6), due to the formation of Mo rich carbides. Carbides could be formed before, at the same time or after $NaCrO_2$. As they were detected under $NaCrO_2$ for all corrosion times investigated, it is not possible to deduce from the experiments where the carburization front is located.

5.2.2. Driving force of dissolution

It was shown that the mass of the stainless steel samples decreased during immersion in liquid sodium for 250 and 500 h (Fig. 2). This means that the stainless steel substrate and/or the chromite scale are dissolved in parallel with the formation of chromite and carbides. The dissolution of the main elements of stainless steel, namely Fe, Ni, Cr and Mn, was already reported to occur in liquid sodium, mainly at low oxygen levels (section 1) [4–7]. The Fe and Ni depletion observed at the metal/oxide interface (Fig. 6) is due to their dissolution in liquid sodium.

Considering the principal elements in the stainless steel chosen (Table 1), the driving force of dissolution is a function of the Fe, Cr, Ni, Mn and Mo concentrations in liquid sodium at equilibrium with steel:

$$M_{steel} \leftrightarrow M_{Na} \tag{16}$$

where M_{steel} means M in solid solution in steel and M_{Na} is M dissolved in liquid sodium, M being Fe, Cr, Ni, Mn or Mo. These equilibrium concentrations can be estimated using the solubility of the elements in liquid sodium and their activities in the steel if one assumes that the solubility of one dissolved element does not change in presence of the others (we made this strong assumption because of a lack of more precise data). The solubility of M in sodium $w_M^{Na,sat}$ (in $\mu g.g^{-1}$) can be found in the literature (Fe [11], Cr [10], Ni [30], Mn [29] and Mo [19]). The solubility of M is defined as the M concentration in liquid sodium at equilibrium with pure stable solid M (body-centered cubic Fe, Cr, Mn and Mo, face-centered cubic Ni at 650 °C). At 650 °C, $w_{Fe}^{Na,sat} = 1.9\ \mu g\ g^{-1}$, $w_{Cr}^{Na,sat} = 0.41\ \mu g\ g^{-1}$, $w_{Ni}^{Na,sat} = 2.4\ \mu g\ g^{-1}$, $w_{Mn}^{Na,sat} = 1.4\ \mu g\ g^{-1}$ and $w_{Mo}^{Na,sat} = 2.3\ \mu g\ g^{-1}$. As in section 5.1.1., the activities of Fe, Cr, Ni, Mn and Mo in austenite were calculated by means of the CALPHAD method in ThermoCalc® with the TCFE8 database. At 650 °C, $a_{Fe} = 0.67$, $a_{Cr} = 0.28$, $a_{Ni} = 0.054$, $a_{Mn} = 0.0043$ and $a_{Mo} = 0.067$, the reference being pure stable metals.

M is present in small quantity in liquid sodium. As currently done in liquid iron [24], Henry's law can be used to express the activity of M in liquid sodium:

$$a_M^{Na} = \gamma_M . x_M^{Na} \tag{17}$$

where γ_M is the Henry's law constant for M and x_M^{Na} is the mole fraction of M in liquid sodium. Assuming that Henry's law is valid for M content lower than or equal to its solubility in liquid sodium, the following equation can be written based on the definition of solubility reminded before (equilibrium between liquid sodium containing the M mole fraction $x_M^{Na,sat}$ and pure M):

$$\gamma_M . x_M^{Na,sat} = 1 \tag{18}$$

And therefore

$$a_M^{Na} = \frac{x_M^{Na}}{x_M^{Na,sat}} \tag{19}$$

As the M content in liquid sodium is low, the activity of M in liquid sodium is also given by:

$$a_M^{Na} = \frac{w_M^{Na}}{w_M^{Na,sat}} \tag{20}$$

Finally, the equilibrium between stainless steel and liquid sodium leads to:

$$a_M = a_M^{Na} = \frac{w_M^{Na}}{w_M^{Na,sat}} \tag{21}$$

Based on this result, the maximum theoretical mass dissolved in liquid sodium (section 2.2) in the CorroNa device is:

$$\max\left(M_{dissolved}^{Na}\right) = \sum_M \frac{M_{Na} \cdot w_M^{Na,sat} \cdot a_M}{N_{samples} \cdot S_{sample}} \tag{22}$$

where M_{Na} is the sodium mass contained in the CorroNa crucible

(2.3 kg), $N_{samples}$ is the number of samples immersed in liquid sodium at the same time (6) and s_{sample} the sample surface area (0.12 dm^2 for 2 faces). For the experiments performed here, it corresponds to 4.5 mg dm^{-2}.

This theoretical mass loss is in good agreement with the one obtained after 250 h of immersion. However, it is twice less than the one measured for samples immersed for 500 h. The data used to determine the solubilities of each element (Fe [11], Cr [10], Ni [30], Mn [29] and Mo [19]) were proposed for pure metals in pure sodium. In our case, oxygen is present in sodium and might have modified these solubilities as suggested for chromium [19] and iron [4,10,11]. The solubilities of chromium and iron are higher in sodium containing oxygen than in pure sodium because some oxides are formed ($NaCrO_2$, Na_4FeO_3). Therefore, the stainless steel under investigation might be dissolved in sodium more than the value calculated above. Consequently, the mass loss measured here is higher than expected in pure sodium.

5.2.3. Cavities formation

In our experiments of corrosion in liquid sodium, cavities were observed at the interface between steel and $NaCrO_2$ scale (Fig. 5).

It is well known that an oxide scale growth at high temperature is sometimes accompanied by a void formation within the metal [31–33]. In such a system, vacancies are created in the metal and the vacancy supersaturation can lead to void formation by nucleation mainly on singularities such as grain boundaries or interfaces. If vacancies are all annihilated at sinks like dislocations, they do not cause void formation within the metal and the oxide/metal interface will translate to consume the metal. Two sources of vacancies are described in the literature. First, the removal of cations from the metal due to the growth of the oxide scale creates cationic vacancies at the oxide/metal interface. Secondly, vacancies can also be created by the so-called Kirkendall effect: when the diffusivities of the different elements in the metal are different from each other, a vacancy flux is obtained in the opposite direction of the flux of the fastest element. This Kirkendall vacancy flux is oriented from the metal/oxide interface to the metal bulk (resp. from the metal bulk to the metal/oxide interface) when the selective oxidized element is the fastest (resp. the slowest) diffusing species in the alloy, leading to pores formation in the bulk of the alloy (resp. under the oxide scale). This is the case of high temperature oxidation of Ni-Cr alloys forming chromia scales in which Cr diffuses much faster than Ni [34] (resp. Ni-Al with Al < 50 mol.%, forming Al_2O_3 scales in which Al diffuses slower than Ni [35]).

In the case studied here, vacancies are created at the steel/$NaCrO_2$ interface by Cr oxidation, carburization (Section 5.2.1) and dissolution of the other elements present in the stainless steel (Section 5.2.2). The vacancies become supersaturated and this leads to the nucleation of the cavities observed (Fig. 5).

In the cross section presented in Fig. 5 (which is representative of the whole sample), the large cavities are 11.5 μm apart from each other. This can be used to estimate the surface density of cavities ($f_{cavities} = 7.6.10^{-3}$ μm^{-2}). Assuming that cavities are only due to chromium departure, the thickness of $NaCrO_2$ formed with the chromium creating the cavities is then given by:

$$e_{NaCrO_2} = V_{cavity} f_{cavities} \frac{\rho_{Cr}}{\rho_{NaCrO_2}} \frac{M_{NaCrO_2}}{M_{Cr}} \quad (23)$$

where V_{cavity} is the mean volume of a cavity supposed to be spherical (7.2 μm^3), ρ_{Cr} the chromium density (7150 kg m^{-3} [36]), ρ_{NaCrO_2} the $NaCrO_2$ density (4360 kg m^{-3} [PDF-2/Release 2012 RDB 04-010-6761), M_{NaCrO_2} and M_{Cr} the $NaCrO_2$ and Cr molar masses (107 and 52 g mol^{-1} [36]), w_{Cr} the Cr mass fraction in the stainless steel studied (0.179, Table 1). Finally, the oxide thickness estimated from the mean cavities volume is 0.2 μm after 250 h immersion. As shown in Figs. 5 and 6, the measured oxide thickness is closed to 1 μm. As a consequence, it can be deduced that the cavities' formation can result from selective oxidation of chromium into sodium chromite. Even if the order of magnitude of the calculated thickness is rough, it can also be said that 1) part of the vacancies created by Cr oxidation or steel dissolution is annihilated at sinks like dislocations leading to the translation of the oxide/metal interface towards the metal bulk and 2) the Kirkendall vacancy flux if it exists is not the main mechanism to explain the cavities formation.

6. Conclusions

The corrosion of an austenitic steel in liquid sodium was investigated in this study. The austenitic steel samples were immersed for 122, 250 and 500 h in liquid sodium with an oxygen content of 189 μg g^{-1} at 650 °C. The steel samples were then characterized by means of complementary techniques, namely scanning electron microscopy, X-ray diffraction, glow discharge optical emission spectroscopy and transmission electron microscopy.

The characterizations showed the formation of a $NaCrO_2$ oxide scale at the steel surface together with underlying M_6C carbide particles rich in molybdenium and iron. The stainless steel substrate and/or the chromite scale were dissolved in parallel with the formation of chromite and carbides. Cavities were observed under the oxide scale within the metal.

The system studied here is composed of liquid sodium containing traces of dissolved oxygen and carbon in contact with a stainless steel. Thermodynamic calculations showed that $NaCrO_2$ and M_6C are equilibrium phases in such a system.

$NaCrO_2$ is formed by the reaction of chromium diffusing from the steel bulk with two components of liquid metal, namely sodium and dissolved oxygen. The Cr composition profiles exhibited a depleted zone due to the formation of $NaCrO_2$. This is a selective oxidation phenomenon, chiefly external, i.e. it occurs on the stainless steel surface. Mo segregates to the steel surface where it reacts with Fe from the steel and C dissolved in liquid sodium that diffuses into the steel matrix according to a carburisation phenomenon.

Stainless steel and liquid sodium are not in thermodynamic equilibrium. The dissolution of stainless steel occurred since the liquid sodium bath is not saturated in the dissolving species. Thermodynamic calculations, using only the solubilities of Fe, Cr, Ni, Mn and Mo proposed in the literature for pure metals in liquid sodium, did not explain the large amount of dissolved steel. This means that the solubilities of these elements are higher in sodium containing oxygen than in pure sodium. One explanation could be that some oxides, such as $NaCrO_2$ or Na_4FeO_3, are formed in liquid sodium, increasing the driving force of dissolution.

As for the cavities, vacancies are created at the steel/$NaCrO_2$ interface by Cr oxidation, carburization and dissolution of the other elements present in the stainless steel. The vacancies become supersaturated and this leads to the nucleation of the cavities observed. Part of the vacancies created by Cr oxidation or steel dissolution is annihilated at sinks like dislocations leading to the translation of the oxide/metal interface towards the metal bulk.

All of this still needs to be elucidated with additional experimental support.

Acknowledgements

The authors are extremely grateful to Jean-Bernard Guillot for fruitful discussions, to the CEA-Generation 4/Structural material

project for part of the financial support, to V. Lorentz for the exposure of the specimen to liquid sodium made in the Corrona-1 test Bench of the CEA-Saclay.

References

[1] R. Dautray, Y. Bréchet, J. Friedel, Les Fluides Caloporteurs Pour Neutrons Rapides, Académie des sciences, EDPscience, Les Ulis, 2014.
[2] J.L. Courouau, F. Balbaud-Célérier, V. Lorentz, T. Dufrenoy, Corrosion by liquid sodium of materials for sodium fast reactors: the CORRONa testing device, in: The Proceedings of the International Congress on Advances in Nuclear Power Plants (ICAPP '11), 2011 paper 11152, Nice, France, May 2-5.
[3] P. Baqué, L. Champeix, A. Lafon, E. Sermet, Some aspects of corrosion of austenitic steels in flowing sodium, in: Liquid Alkali Metals Proceedings of the International Conference Organized by the British Nuclear Energy Society, Nottingham University, 1973, pp. 223–231. April 4-6, The British Nuclear Energy Society, London, 1973.
[4] J.R. Weeks, H.S. Isaacs, Corrosion and deposition of steels and nickel-base alloys in liquid sodium, in: Advances in Corrosion Science and Technology, vol. 3, Plenum Press, New York, London, 1973, pp. 1–66.
[5] T. Suzuki, I. Mutoh, T. Yagi, Y. Ikenaga, Sodium corrosion behavior of austenitic alloys and selective dissolution of chromium and nickel, J. Nucl. Mater. 139 (1986) 97–105.
[6] T. Gnanasekaran, R.K. Dayal, Liquid metal corrosion in nuclear reactor and accelerator driven systems, in: D. Féron (Ed.), Nuclear Corrosion Science and Engineering, Woodhead Publishing Limited – Cambridge, Philadelphia, 2012, pp. pp.301–328.
[7] E. Yoshida, T. Furukawa, Corrosion issues in sodium-cooled fast reactor (SRF) systems, in: D. Féron (Ed.), Nuclear Corrosion Science and Engineering, Woodhead Publishing Limited – Cambridge, Philadelphia, 2012, pp. 773–806.
[8] B.H. Kolster, Mechanism of Fe and Cr transport by liquid sodium un non-isothermal loop system, J. Nucl. Mater. 55 (1975) 155–168.
[9] A.W. Thorley, J.A. Bradsley, Structural changes in materials exposed to liquid sodium, J. R. Microsc. Soc. 88 (1968) 431–447.
[10] R.M. Singer, A.H. Fleitman, J.R. Weeks, H.S. Isaacs, Measurements of the solubility of iron and chromium in sodium, in: Corrosion by Liquid Metals, Proceedings of the Sessions on Corrosion by Liquid Metals of the 1969 Fall Meeting of the Metallurgical Society of AIM, October 13-16, vol. 1970, Plenum Press, Philadelphia, Pennsylvania, New-York – London, 1969, pp. 561–576.
[11] W.P. Stanaway, R. Thompson, Solubility of metals, iron and manganese in sodium, in: Richland Washington, J.M. Dahlke (Eds.), Second international Conference on liquid metal technology in energy production – Proceedings Part 2, April 20-24, 198, 1980, pp. 18.54–18.61.
[12] B.H. Kolster, L. Bos, Sodium corrosion in a total molybdenum loop system: construction, experience and results, in: Liquid Metal Engineering and Technology, The British Nuclear Energy Society, London, 1984, pp. 235–242.
[13] I.W. Cavell, M.G. Nicholas, Some observations concerned with the formation of sodium chromite on AISI 316 exposed to oxygenated sodium, J. Nucl. Mater. 95 (1980) 129–144.
[14] A.G. Crouch, P.R. Bussey, Corrosion of ferritic steels in flowing sodium, in: Ferritic Steels for Fast Reactor Steam Generators, The British Nuclear Energy Society, London, 1978, pp. 258–263.
[15] A.G. Crouch, The growth and stability of sodium chromite and its influence on corrosion, in: J.M. Dahlke, Richland Washington (Eds.), Proceedings of the Second International Conference on Liquid Metal Technology in Energy Production, Part 1, April 20-24, 1980, 1980, pp. 3–43 to 3-51.
[16] S.H. Shin, J. Lee, J.H. Kim, J.H. Kim, Mechanism of corrosion of 9Cr and 12Cr ferritic/martensitic steels under oxygen-saturated sodium, Curr. Sci. (2016). https://doi.org/10.1016/j.corsci.2016.09.001.
[17] P.L.F. Rademakers, B.H. Kolster, Corrosion of various ferritic steels in an isothermal sodium loop system, J. Nucl. Mater. 97 (1981) 309–318.
[18] J.L. Courouau, V. Lorentz, M. Tabarant, S. Bosonnet, F. Balbaud-Célérier, Corrosion by oxidation and carburization in liquid sodium at 550°C of austenitic steels for sodium fast reactors, in: Proceeding of International Conference on Fast Reactors and Related Fuel Cycles: Safe Technologies and Sustainable Scenarios (FR13), 4–7 march 2013. Paris, France.
[19] H.U. Borgsted, C.K. Mathews, Applied Chemistry of the Alkali Metals, Plenum Press, New-York, 1987 p.191 and p.184.
[20] B.J. Shaiu, P.C.S. Wu, P. Chiotti, Thermodynamic properties of the double oxide of Na_2O with the oxides of Cr, Ni and Fe, J. Nucl. Mater. 67 (1977) 13–23.
[21] N.P. Bhat, H.U. Borgstedt, Corrosion behaviour of structural materials in sodium influenced by formation of ternary oxides, Werkstoffe Korrosion 39 (1988) 115–123.
[22] D.R. Fredrickson, M.G. Chasanov, The enthalpy of sodium oxide Na_2O to 1300 K by drop calorimetry, J. Chem. Therm. 5 (1973) 485–490.
[23] J.D. Noden, A general equation for the solubility of oxygen in liquid sodium, J. Br. Nucl. Energy Soc. 12 (1) (1973), 57-62 and 329–331.
[24] A. Rist, M.-F. Ancey-Moret, C. Gatellier, P.-V. Riboud, Équilibres thermodynamiques en sidérurgie, Techniques de l'Ingénieur, M 1730 (1974) 1–33 (in French).
[25] A.D. Le Claire, The analysis of grain boundary diffusion measurements, Br. J. Appl. Phys. 14 (1963) 351–366.
[26] I. Kaur, Y. Mishin, W. Gust, Fundamentals of Grain and Interphase Boundary Diffusion, Wiley, Chichester, 1995.
[27] H. Mehrer, Diffusion in solids, in: M. Cardona, P. Fulde, K. von Klitzing, H.-J. Queisser, R. Merlin, H. Störmer (Eds.), Springer series in Solid-state Sciences, Springer, Berlin, 2007.
[28] M. Rivollier, Corrosion des aciers austénitiques par le sodium liquide en présence d'oxygène, PhD Thesis, CentraleSupélec, 2017 (in French).
[29] W.P. Stanaway, R. Thompson, The solubility of transition metals, Mn and Co in liquid sodium, in: H.U. Borgstedt (Ed.), Material Behavior and Physical Chemistry in Liquid Metal System, Plenum Press, New York – London, 1982, pp. 421–427.
[30] S.P. Awasthi, H.U. Borgstedt, An assessment of solubility of some transition metals (Fe, Ni, Mn and Cr) in liquid sodium, J. Nucl. Mater. 116 (1983) 103–111.
[31] H.E. Evans, Cavity formation and metallurgical changes induced by growth of oxide scales, J. Mater. Sci. Technol. 4 (1988) 1089–1098.
[32] D.J. Young, High Temperature Oxidation and Corrosion of Metals, Elsevier, Amsterdam, 2008.
[33] C. Desgranges, F. Lequien, E. Aublant, M. Nastar, D. Monceau, Depletion and voids formation in the substrate during high temperature oxidation of Ni-Cr alloys, Oxid. Met. 79 (2013) 93–105.
[34] E. Schmucker, C. Petitjean, L. Martinelli, P.-J. Panteix, B. Lagha, M. Vilasi, Oxidation of Ni-Cr alloy at intermediate oxygen pressures. II. Towards the lifetime prediction of alloys, Curr. Sci. 111 (2016) 467–473.
[35] M.W. Brumm, H.J. Grabke, Oxidation behaviour of Ni-Al – II. Cavity formation beneath the oxide scale on NiAl of different stoichiometries, Corrosion Sci. 34 (1993) 547–561.
[36] David R. Lide, CRC Handbook of Chemistry and Physics, 90th ed., CRC Press Inc, 2009, ISBN 978-1-420-09084-0, 2804 p.